3-D body-wave tomography from the seismic ambient noise recorded by a dense array in the Dehdasht area, Iran

Ali Riahi, Zaher-Hossein Shomali, Anne Obermann, Ahmad Kamayestani

Geophysical Journal International

Geophys. J. Int. (2023) **234,** 1332–1341
Advance Access publication 2023 March 27
GJI Seismology

https://doi.org/10.1093/gji/ggad135

3-D body-wave tomography from the seismic ambient noise recorded by a dense array in the Dehdasht area, Iran

Ali Riahi [1,2] Zaher-Hossein Shomali,[3] Anne Obermann [4] and Ahmad Kamayestani[5]

[1]*Institute of Geophysics, University of Tehran (IGUT), Tehran, PO Box* 14155-6466, *Iran E-mail: riahi@ipgp.fr*
[2]*Institut de Physique du Globe de Paris (IPGP), Université Paris Cité, Paris,* 75238, *France*
[3]*Institute of Geophysics, University of Tehran (IGUT), PO Box* 14155-6466, *Tehran, Iran*
[4]*Swiss Seismological Service (SED), ETH Zurich, Zurich,* 8092, *Switzerland*
[5]*Department of Geophysics, Science and Research Branch, Islamic Azad University, PO BOX* 14515-775, *Tehran, Iran*

Accepted 2023 March 24. Received 2023 March 13; in original form 2022 July 18

SUMMARY

The strong attenuation of the thick sedimentary layers in the Dehdasht region, Iran, renders active seismic exploration surveys difficult. The imaging of the existent limestone reservoirs is limited to the shallow subsurface due to the strong attenuation of seismic waves. Here, we discuss a different approach to imaging the subsurface using body waves extracted from the cross-correlation of the seismic ambient wavefield. We discuss the technical challenges to extracting clear *P*-wave arrivals from the seismic ambient wavefield of a dense 3-component seismic array deployed in the Dehdasht basin. We invert the data for the 3-D *P*-wave velocity structure and compare the velocity model with results from the 2-D active seismic surveys in the area. The results show the potential of using body waves extracted from the seismic ambient wavefield for imaging purposes in highly attenuating areas.

Key words: Tomography; Body waves; Seismic interferometry; Seismic noise; Sedimentary basin processes.

1 INTRODUCTION

Since the discovery that seismic ambient noise carries valuable information about the subsurface (Shapiro & Campillo 2004), numerous studies have extracted surface waves from the seismic ambient wavefield to image the subsurface (e.g. Sabra *et al.* 2005; Abdetedal *et al.* 2015; Köhler *et al.* 2015; Shomali & Shirzad 2015; Obermann *et al.* 2016, 2019; Singer *et al.* 2017; Lehujeur *et al.* 2018; Planès *et al.* 2020). Surface waves have dominant amplitude arrivals in empirical Green's functions (Shapiro *et al.* 2005), allowing for easy extraction. Extracting body waves is more challenging given the low energy arrivals. Only a handful of studies extracted diving *P* waves in local distances (e.g. Roux *et al.* 2005; Zhang & Gerstoft 2014; Nakata *et al.* 2015, 2016; Riahi *et al.* 2021) or reflected *P* waves (e.g. Draganov *et al.* 2009; Dantas *et al.* 2018) from the ambient wavefield; as well as in teleseismic distances (e.g. Poli *et al.* 2012; Boué *et al.* 2013; Spica *et al.* 2017; Retailleau *et al.* 2020). Due to their higher frequency content, using body waves can result in higher resolution images of the subsurface when compared to surface waves (Nakata *et al.* 2015).

Here, we extract body waves from a dense seismic array in the Dehdasht basin in southwestern Iran. The Dehdasht area is located in the southern Dezful Embayment in the Zagros fold-and-thrust belt, a rich petroleum area that contains around 8 per cent of global hydrocarbon reservoirs (Bordenave & Hegre 2005). Several geological features suggest that the Dehdasht basin also hosts petroleum reservoirs. The Dehdasht basin is a small and lowland area that is enclosed by the Kuhe Siah anticline in the NE and the Khaviz anticlines in the SW, exposing Sarvak and Asmari formations, respectively (Macleod & Akbari 1970; Liewellyn 1973). The Dehdasht area contains both compressive and halokinetic sequences that complicate the tectonics and their interpretation in the region (Najafi *et al.* 2018; Lashgari *et al.* 2020).

A particular challenge is that the Dehdasht basin consists of up to 6 km thick evaporates, the Gachsaran formation, overlaying the potential reservoir host rocks (Heydarzadeh *et al.* 2020, 2021). Several 2-D active seismic profiles from the National Iranian Oil Company (NIOC) crossed the Dehdasht area. However, the strong attenuation of the Gachsaran formation limited the survey depth to around 3 km and failed to image deeper, that is the potential Asmari reservoir.

From August 2016 to July 2017, NIOC deployed 119 temporary 3-components seismic stations with an interstation spacing of around 2 km in 10 m deep boreholes across the Dehdasht region (Salinas *et al.* 2019; Fig. 1). The stations consist of broad-band seismic sensors, SARA SS-BHV and R-sensors CME-4211, with corner frequencies of 0.2–50.0 Hz and 0.1–50.0 Hz, respectively. Spidernano digitizers were used for all stations.

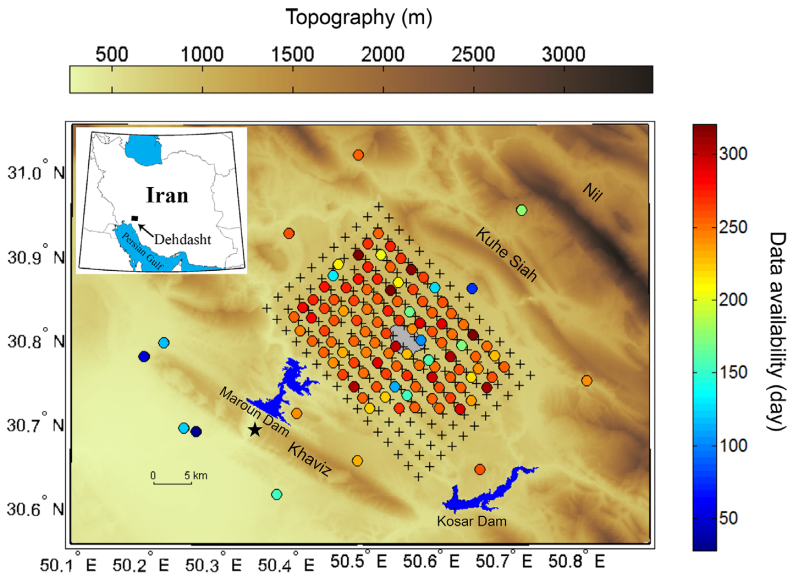

Figure 1. The location and data availability of the Dehdasht array. The circles show the locations of the 119 seismic stations, colour-coded for data availability. The locations of the grid nodes are marked by crosses. The city of Dehdasht is illustrated in grey in the middle of the array. The black star refers to the position of the well.

Using part of this database, Riahi *et al.* (2021) showed that body and surface waves could be simultaneously extracted using the polarization approach of Takagi *et al.* (2014). With a summation of the ZR and RZ components, the *P*-wave contribution could be enhanced and the Rayleigh wave component eliminated.

In this study, we modify and expand the work of Riahi *et al.* (2021) and perform 3-D seismic tomography of the Dehdasht area by inverting the time arrivals of the retrieved diving *P* wave. We first evaluate the noise source characteristics and describe the extraction of the *P* wave from the seismic ambient wavefield (Section 2) and outline the tomography (Section 3), before we discuss our results (Section 4).

2 P-WAVE RECONSTRUCTION FROM THE SEISMIC AMBIENT WAVEFIELD

The *P*-wave reconstruction from the seismic ambient wavefield is a challenging endeavour. Since localized noise sources can bias the reconstruction, we first analyse the noise sources in detail (Section 2.1). Then, we separate surface and body waves (Section 2.2) and finally separate the first arriving *P* waves (Section 2.3).

2.1. Dominant ambient noise sources

Riahi *et al.* (2021) showed with beamforming analysis that the noise source distribution in the Deshdasht area is uneven for the frequencies of interest (around 0.7–1.2 Hz). The most dominant noise sources are the Persian Gulf, located approximately 80 km south of the area, and two concrete dams: the Maroun dam in the SW and the Koser dam in the SE in the vicinity of the array (Fig. S1).

Here, we further evaluate the dominant noise sources and the directional intensity in small time segments to rule out a remaining bias for the *P*-wave reconstruction using the polarization approach by Takagi *et al.* (2018). This approach utilizes the separation of surface wave and *P* wave through the imaginary and real parts of the cross-spectra. The imaginary part of the cross-spectra between the vertical and two horizontal components is related to the azimuthal of elliptical Rayleigh energy, and the real part is related to the linear *P* wave.

We apply the method to 15 continuous days of data. First, we cut the waveforms into 15 min windows for each station. Next, we calculate the cross-spectra between different components for each segment, using Welch's method (REF). We only consider the frequency band of 0.7–2.0 Hz, since we know that the *P* wave can be retrieved in this frequency range (Riahi *et al.* 2021). The backazimuth of the dominant noise source of the *P* wave is calculated by the arctangent between the mean of the real part of vertical-north and the mean of the real part of vertical-east cross-spectra. The imaginary part is used for the Rayleigh wave. The directional intensity amplitude of the *P* wave is estimated by the square root of the mean of vertical-north and the mean of vertical-east cross-spectra. The real and imaginary parts of cross-spectra relate to the directional intensity of *P* and Rayleigh waves, accordingly.

The results are shown in Fig. 2, in which each dot corresponds to a time segment. We select two stations (black circles; Fig. 2a) near Dehdasht city (labelled A) and the other station far from the potential noise sources (labelled B) that may include incident plane waves. The backazimuths and directional intensity ratios for both sites are illustrated in Figs 2(b)–(d) and (e)–(g), respectively. The arctangent in the equation leads to an uncertainty of 180° for the backazimuths. An average from the results of all the stations of the array is calculated, which is shown in Figs 2(h)–(j).

Figs 2(c) and (f) show the dominant noise source backazimuth, mostly in the direction of around 200–300° (±180°) for the Rayleigh energy. The dominant *P* wave is mostly emitted from the backazimuth of about 200–250° to station 'B' (Fig. 2e), while there are directional variations in the station 'A' with higher density around 200° (±180°; Fig. 2b). These variations are likely caused by the local cultural noise of Dehdasht city. The averaged backazimuth shows less deviation, mostly around 200° (±180°) for *P*-energy and around 150–200° (±180°) for Rayleigh energy (Figs 2h and i). These directions agree with the location of the Persian Gulf and the concrete dams (Figs S1c–e).

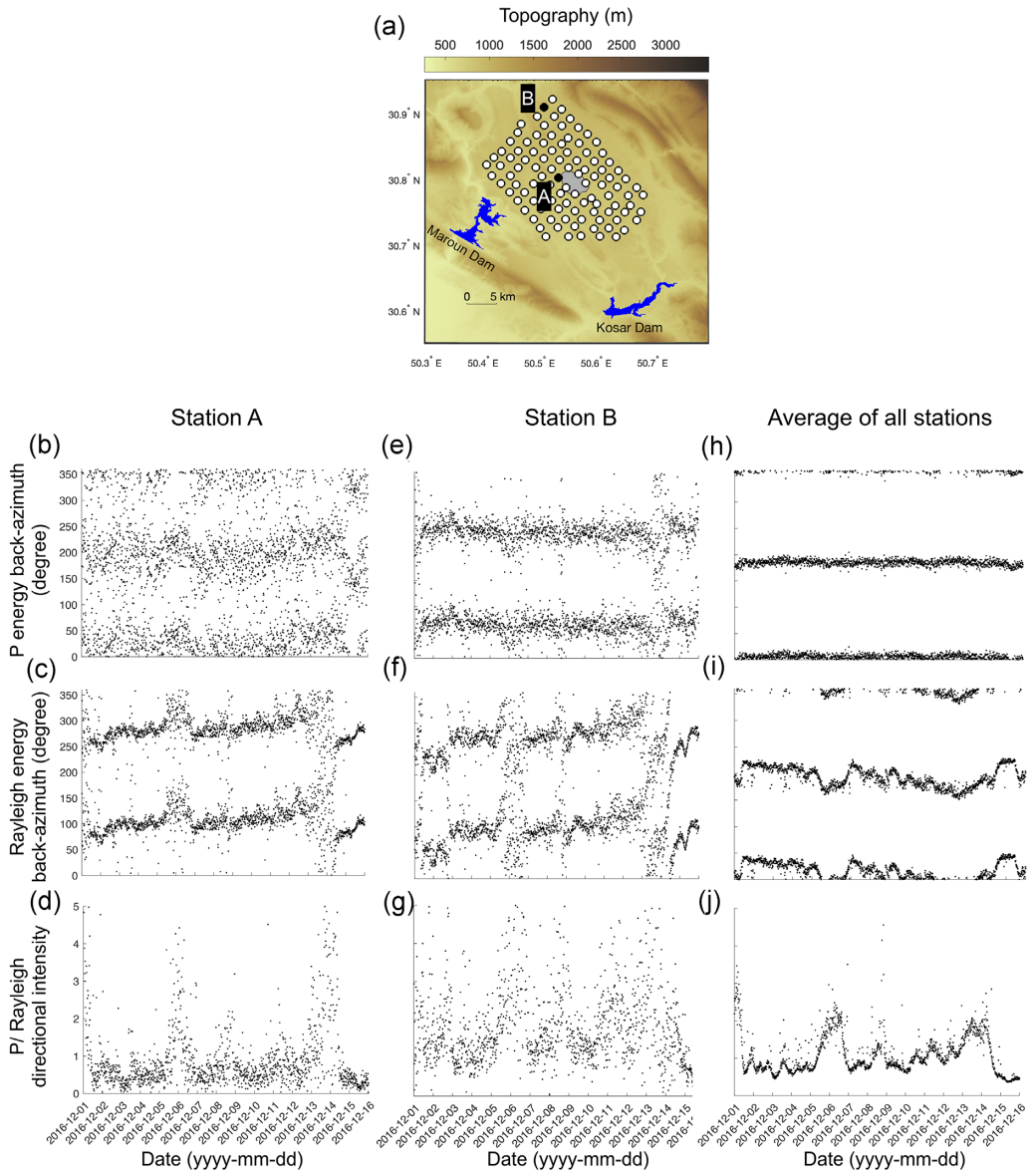

Figure 2. The polarization estimation, backazimuth of the dominant ambient noise sources of the *P* and Rayleigh waves, and the amplitude ratio between them. (a) The location of the selected stations are marked by black circles, labelled by 'A' and 'B'. (b–d) The dominant backazimuth of *P*- and Rayleigh waves of seismic noise sources for station 'A' and the directional intensity. The dots refer to each 15 min segment. There is an uncertainty of 180° for the backazimuths. The direction of 270° refers to the west side of the array. (e–g) Same as (b–d) but for station 'B', and (h–j) same as (b–d) but for an average of all stations that are denoted in (a) by circles.

The directional intensity ratio between dominant noise sources of *P* and Rayleigh waves for station 'A', station 'B', and the average of all stations are illustrated in Figs 2(d), (g) and (j). These ratios show that the contribution of the Rayleigh wave noise usually dominates.

2.2 Separation of surface and body waves

Using part of the Dehdasht data set, Riahi *et al.* (2021) reconstructed a clear *P* wave from the ambient wavefield with the bin-stacking method (Ruigrok 2014; Nakata *et al.* 2015; Nakata & Nishida 2019). For our 3-D tomographic purposes, we modify this approach since the bin-stacking strongly averages lateral variation and does not warrant enough 3-D phases for picking.

First, we estimate the daily empirical Green's functions by calculating the cross-coherency of different component pairs (ZZ, ZR, RZ and TT). We work in the frequency band of 0.7–2.0 Hz, which warrants a flat instrument response. Here, we are only interested in the time-antisymmetric parts of the (ZR + RZ)/2 component, as they emphasize the *P* wave part of Green's function and eliminate the Rayleigh energy. The ZR and RZ components are represented by the first order of the Bessel function, which indicates the asymptote to zero amplitude at zero distance. For *P*-wave incidence, these components are purely imaginary (Takagi *et al.* 2014). Since the energy partition between surface and body waves often depends on the noise level (Takagi *et al.* 2018), we obtain more enhanced results using only selected days with high SNR for the bin-stack (250 m) of the (ZR + RZ)/2 components between all virtual sources and all

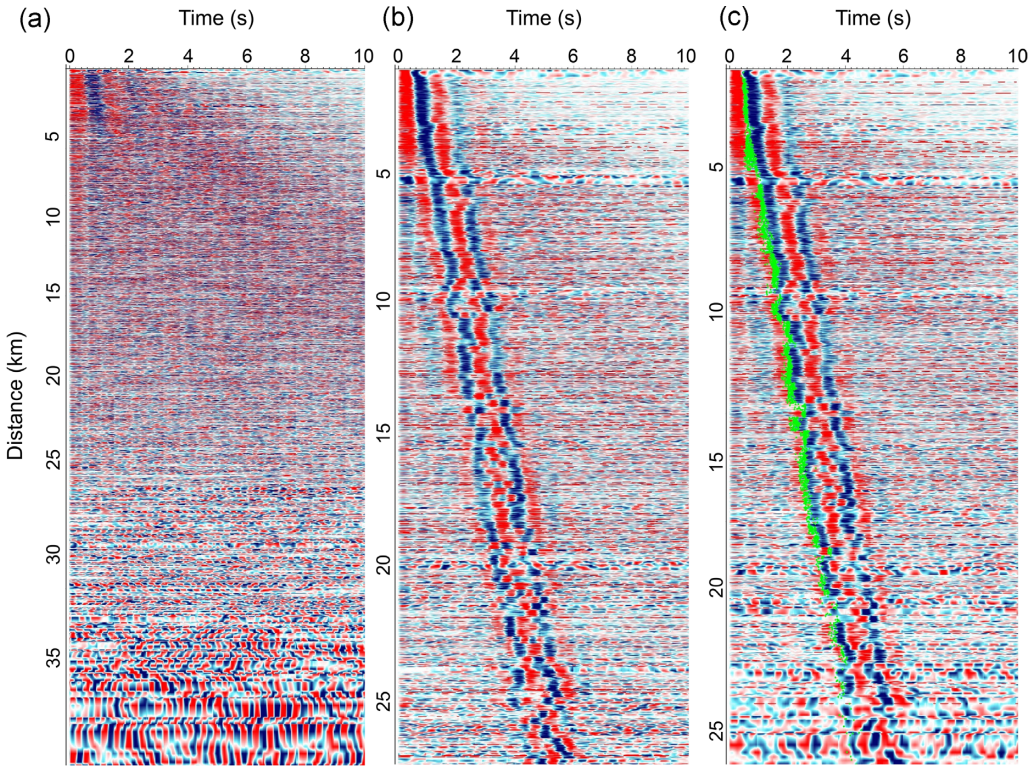

Figure 3. (a) Distance-arrival time representation of the final estimated empirical Green's functions after applying the ACF approach to all traces. Note that the *Y*-axis is sorted by the interstation distance between virtual sources and virtual receivers. The amplitude of each trace has been normalized. The warm and cold colours denote positive and negative amplitudes, respectively. (b) Same as (a), but the ACF is only applied to the daily selected traces with CC > 0.8. The coherent moveouts of the arrivals show the reconstructed *P* wave and the later arrivals. (c) Same as (b), but only the selected empirical Green's functions for manual picking are illustrated. The picked *P* phases are shown by green dots. (a), (b) and (c) contain 6149, 3559 and 2855 traces, respectively.

virtual receivers (Fig. S2a).

Next, we apply a narrow Gaussian window with a length of 1.4 s to the bin-stack traces, where the P-phase moveout is observable corresponding to the distance. This window isolates the retrieved *P* wave and mutes noise and artefact pulses. This step is important since there are localized high-energy influxes in the Dehdasht area, overlapping with our frequency band of interest, resulting in prominent spurious arrivals that could be mistaken for the *P* wave (Fig. S2b; Forghani & Snieder 2010; Pedersen & Colombi 2018; Riahi *et al.* 2021).

2.3 Extraction of *P* phases

The uneven distribution of noise sources in the Dehdasht area can result in the existence of localized noise sources outside the end-fire lobes, impeding the *P*-wave reconstruction for certain days or station pairs. We can avoid the use of such traces by filtering the data with ideal 'filter traces' that contain well reconstructed *P* waves. Only if the correlation coefficient (CC) between the filtered trace and the isolated *P* phase from the individual trace is CC > 0.8, the trace is kept (Nakata *et al.* 2015). Only around 5 per cent of the data pass these very selective filtering criteria, reducing the final number of available daily traces from 1300 000 to around 50 000 daily traces. The exact number of daily traces varies hereby for each station couple but is below 50 for the vast majority of couples (95 per cent).

We further boost the weak *P* phases by suppressing the incoherent pulses with an Adaptive Covariance Filter (ACF) approach (Samson & Olson 1981; Du *et al.* 2000; Nakata *et al.* 2015). The ACF is controlled by three parameters: the length of the time window, overlapping, and harshness. All time-series are divided into several equal length subtraces according to a specific time-window and overlapping; then the ACF is applied to each subtrace of all available daily data sets. The coherency of the ACF approach is controlled by harshness. We apply the ACF to (ZR + RZ)/2 components for all station couples with a time window = 1 s, overlapping = 45 per cent, and harshness = 1.5. We test the application of the ACF on all available daily traces (Fig. 3a) and on selected daily traces only (Fig. 3b) that show a CC > 0.8, resulting in a suppression of incoherent energies. While the stack of all daily traces yields unsatisfactory results, the stack of selected days only reveals a clear moveout of the reconstructed *P* phase (zero moveout) and a later arrival. The later arrival might be an associated PP phase or another converted phase. Note that the amplitude ratio of the first to second arrivals is generally >1 in short distances (< ∼6 km), but this ratio tends to be <1 in far distances (> ∼6 km). The extraction of the *P* phase in Fig. 3(b) and the absence of it in Fig. 3(a) show the importance of the selective filtering steps for the body-wave extraction. Note that the minimum interstation distance in Fig. 3 is around 2 km. The amplitude of each trace is normalized for better illustration of the low-amplitude *P*-wave energy.

3 BODY-WAVE TOMOGRAPHY

For the tomography, we focus on the dense rectangle of stations in the centre of the Dehdasht area, since the locations of the outer stations of the array could not provide sufficient ray coverage for a detailed tomography.

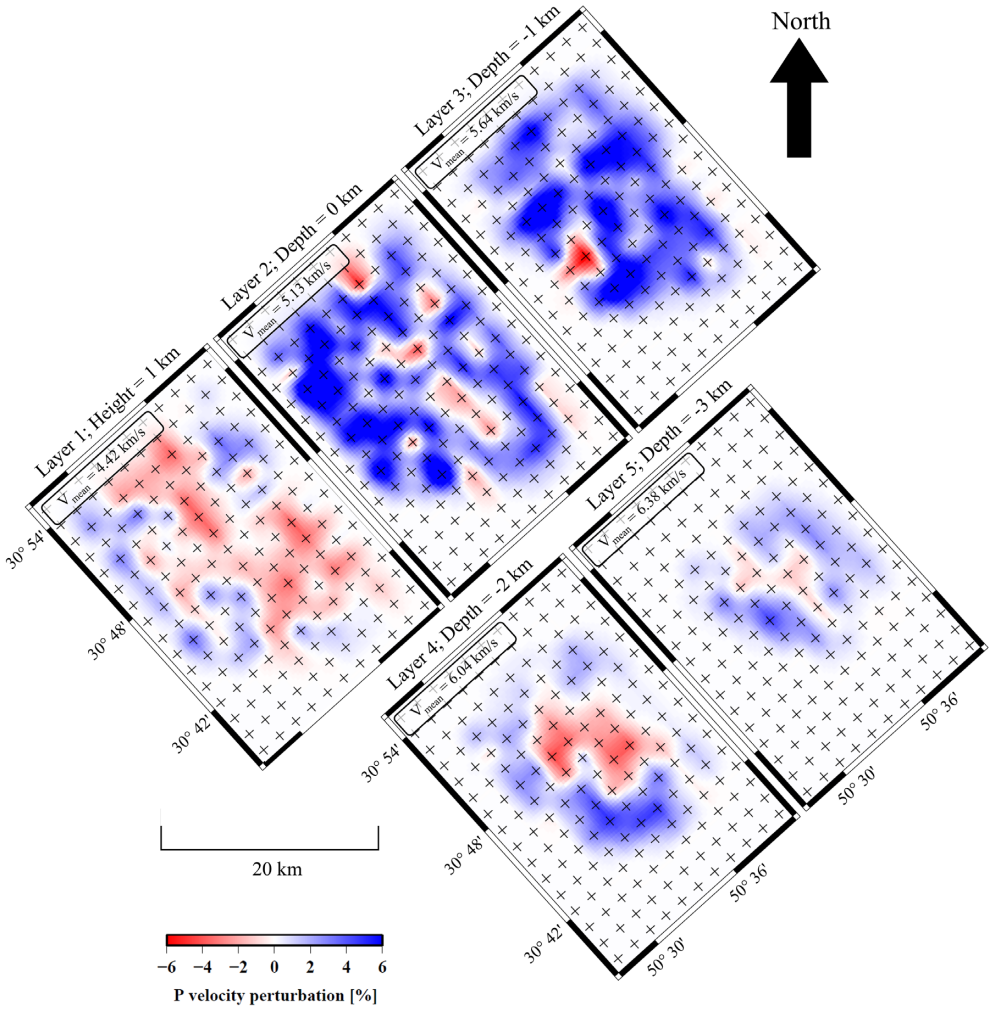

Figure 4. Horizontal slices showing the final *P*-wave velocity perturbation relative to the 1-D initial model (black curve of Fig. S4b). The crosses denote the nodes.

3.1. *P*-phase picking

The *P*-wave phases are picked manually on the time–distance plots. We eliminate traces with unclear *P* phases as well as outliers of more than 0.12 standard deviation. Picking coherent phases in the time–distance plots is important, as despite the enhanced pre-processing, only a minority of individual traces (35 per cent) show dominant *P*-wave onsets. Accurate picking of the first arrivals is hence done on time–distance plots, where a coherent moveout of the *P* wave is present. The final arrival times are illustrated in Fig. 3(c) by green dots. We transform the traces of Fig. 3(c) to the time intercept—slowness (τ–p) domain (Fig. S3; McMechan *et al.* 1982) and observe a coherent wavefield with horizontal slowness of around 0.15 s km^{-1} in the time intercept of up to 3.5 s. This observation is in agreement with the *P*-arrival picks marked by green dots in Fig. 3(c). Since some traces are spaced larger than half of the wavelength, the spatial aliasing may lead to some artefact lines as depicted throughout Fig. S3.

3.2. Inversion for a 3-D *Vp* structure

We use SIMULPS14 (Thurber 1983, 1993; Eberhart-Phillips 1993) to invert a 3-D velocity structure. SIMULPS14 can simultaneously invert both source locations and velocity structure. Here, we only invert the velocity structure, as the virtual source locations are known. We use a horizontal grid of 2 km and a vertical spacing of 1 km down to 4 km depth. We align the grid with the array geometry (black crosses, Fig. 1). The optimum damping value is determined from the trade-off between data variance and model variance (Eberhart-Phillips 1986). We selected a damping value of 15 for this inversion (Fig. S4a).

NIOC provided us with two 1-D *P*-wave velocity models; a 1-D *P*-wave model resultant from well logging (well location indicated with a black star in Fig. 1; blue curve, Fig. S4b) and a 1-D *P*-wave model from an active field survey (red curve, Fig. S4b). NIOC provides us velocity models that were smoothed and interpolated with a constant depth resolution of 200 m. Since the vertical spacing in this study is fixed at 1 km, we derive the block model of Fig. S4(b) according to the spacing of the vertical nodes. Although the 1-D *P*-wave velocity model agrees well with our picked arrival times from far distances ($>\sim$2 km), the velocity model from the well is accurate for near distance arrivals ($<\sim$2 km). This can be explained by the different structures between the drilling point of the well and the seismic surveyed area, especially in shallow depths. We hence decided to use an average of these two models as the initial reference velocity model for the inversion (black curve in Fig. S4b).

SIMULPS14 controls weighting as a function of arrival time residual. We set an appropriate time residual weighting to reduce the

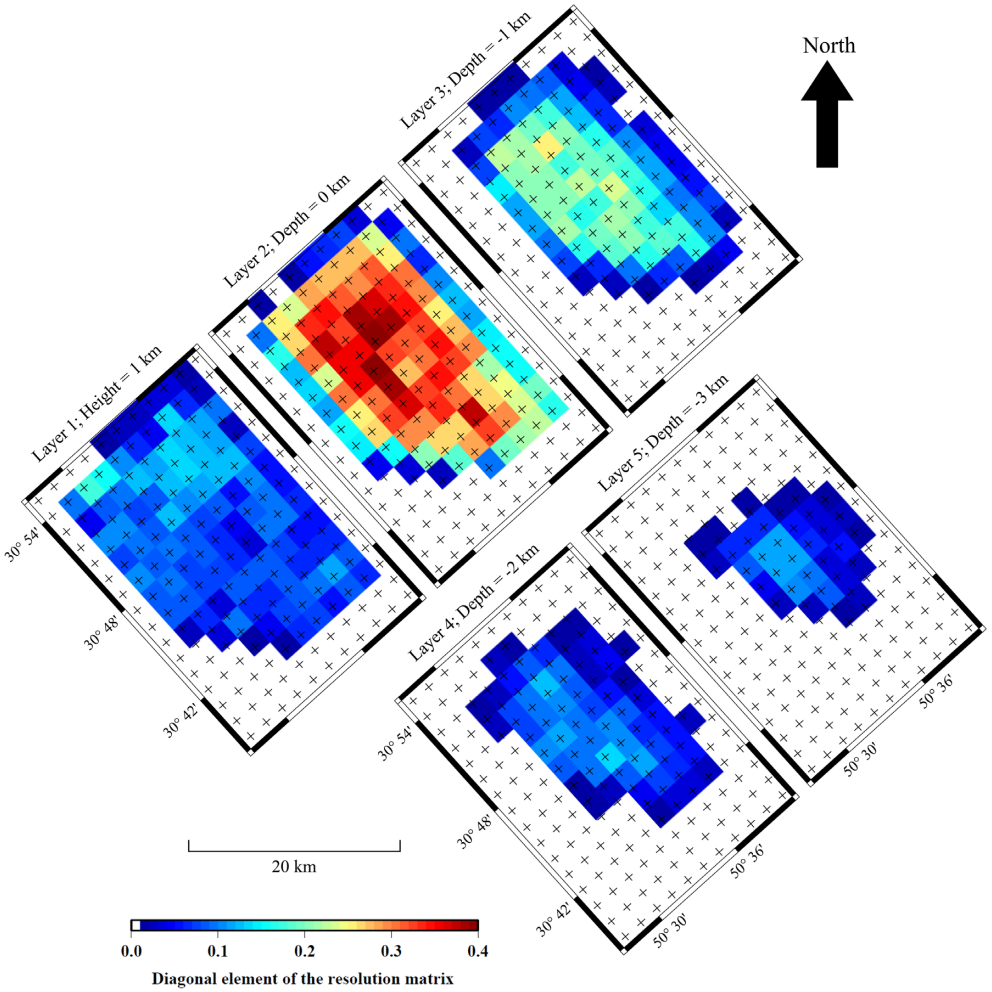

Figure 5. Horizontal slices showing the diagonal element of the resolution matrix of the tomography output. The crosses denote the nodes. The inversion results of the nodes with RDE <0.1 are not reliable.

portion of any miss-reconstructed *P*-phases or any miss-picking in the results. In detail, we set weighting 1.0 below time residual =0.0, weighting 0.0 above time residual =3.0, and weighting 0.02 at time residual =0.2, with linear tapers between them.

We then invert the station delay to compensate for near-surface anomalies beneath the stations and phase differences. The corrected delay for each station is illustrated in Fig. S5. Note that the picked *P*-wave first arrivals (Fig. 3c, green dots) may include some bias due to the phase differences. Fig. 3(c) shows a gentle slope (small slowness) in the offset shot-gather less than 5 km, which makes its physical interpretation difficult. The station delay correction repairs such systematic measurement bias as well as the effect of shallow structure.

As a next step, the velocity structure is inverted. The results are shown for horizontal slices at 1 km height and 0, 1, 2 and 3 km depth (Fig. 4). The corresponding resolution of the diagonal elements (RDE) and Derivative Weight Sum (DWS) are illustrated in Figs 5 and S6, respectively. The high density of the rays at the centre of the array can provide the feasibility of regularization according to the ray density (e.g. Barmin *et al.* 2001).

Additionally, three vertical profiles are shown in Fig. 6 that coincide with active seismic survey lines from NIOC. The smoothed perturbation of the *P*-wave velocity at zero depth in Fig. 4 shows a high velocity area on the west side of the array, corresponding to an absolute velocity of around 5.5 km s^{-1}. From the horizontal depth slices at 2 and 3 km (Figs 4c and d), we observe a low velocity area (around 6 km s^{-1}) in the middle of the array and higher velocities (around 6.5 km s^{-1}) towards the basin edges. The wavelength of the *P* wave with a dominant frequency of 1 Hz is around 5 km, which provides an estimation of the ray's penetration depth.

3.3. Resolution assessment

To assess the resolution of the tomographic inversion, we conduct a 3-D checkerboard test. Arrival times are simulated based on a velocity model with alternating ±15 per cent velocity perturbation (Fig. S7). We use the same initial velocity model and grid for the test as for the final model. The velocity structure is well recovered in the centre of the array, worsening towards the boundaries. Lateral smearing can be observed.

We also compute the DWS of the final results and study the RDE of both main results (Fig. 5) and checkerboard outcomes. The DWS and RDE of the three illustrated profiles in Fig. 6 are shown in Fig. 7. The DWS estimates the total ray length that affects the model parameter (Thurber & Eberhart-Phillips 1999). The RDE evaluates range from 1 for perfect resolution to 0 in places of no resolution (Toomey & Foulger 1989). Comparison of recovered checkerboard anomalies (Fig. S7) and the corresponding resolution distribution

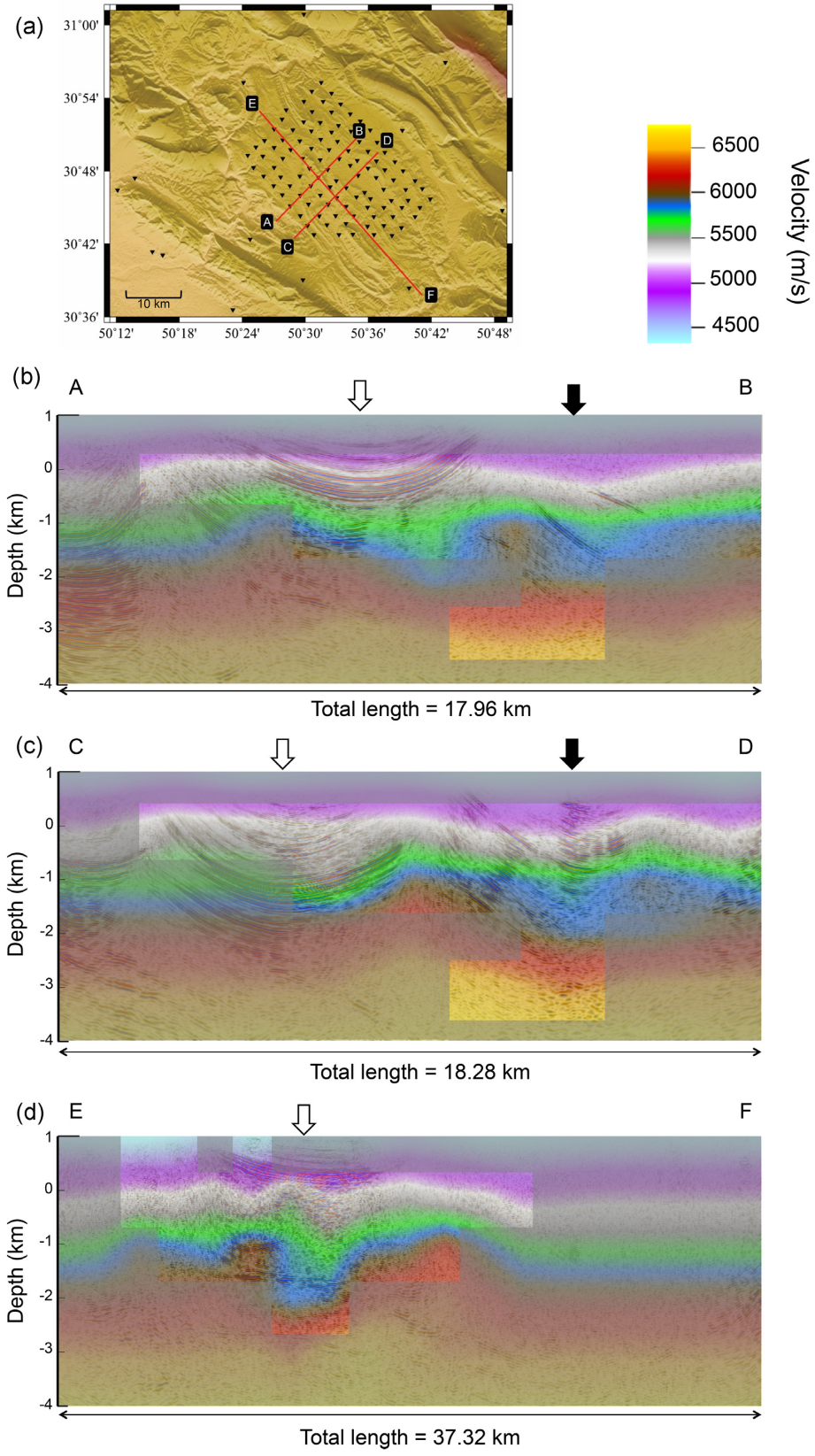

Figure 6. Vertical-section comparison between the absolute *P*-velocity from this study and the analysed active field data from NIOC. (a) The location of three profiles 8203, 8204 and 8211 that cross the centre of the Dehdasht array, are labelled by A-B, C-D and E-F, respectively. The triangles denote the station locations. (b–d) The active field results overlaid with coloured *P*-velocities with appropriate agreement in low-velocity synclines. The white and black arrows refer to the west and east side synclines, respectively. The areas with unreliable resolution (RDE < 0.1) are masked.

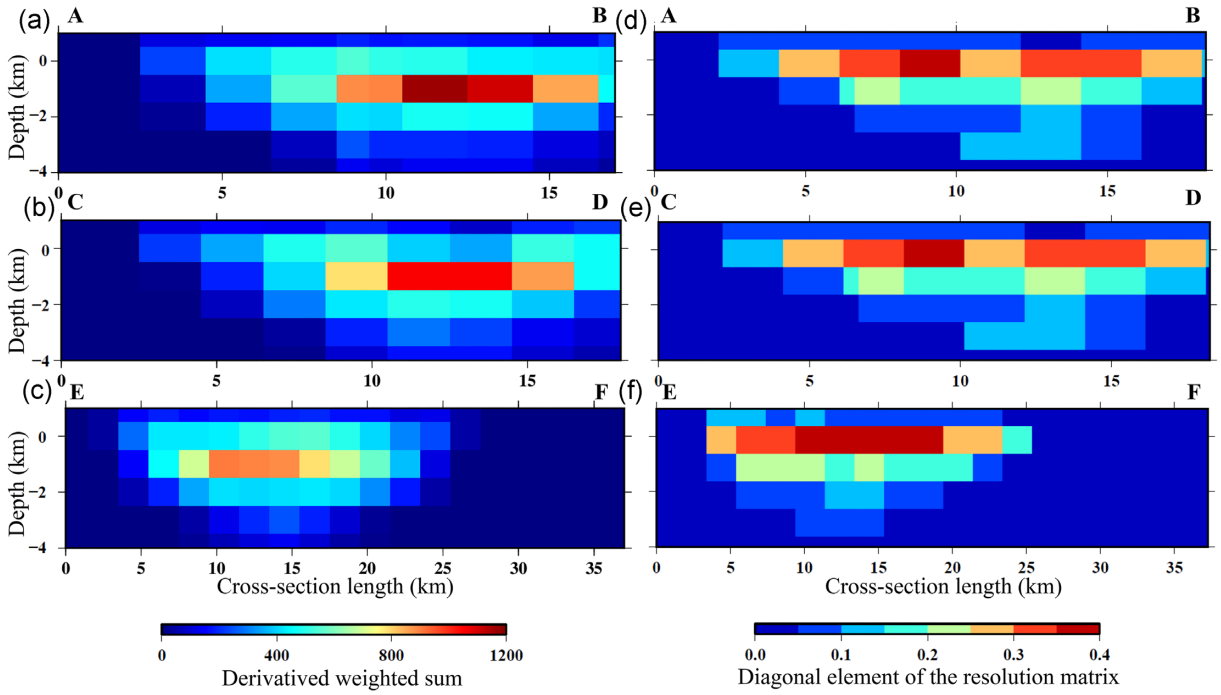

Figure 7. (a–c) Derivative weight sum and (d–f) diagonal elements of the resolution matrix, corresponding to vertical-sections A-B, C-D and E-F of Fig. 6. The regions with RDE >0.1 are resolved.

indicates that the area with RDE >0.1 can reliably image structures with velocity perturbation of around ±4 per cent.

Consequently, investigation of Fig. 5 with consideration of the zones with RDE >0.1 shows that the nodes of the horizontal slice at zero depth have the highest resolutions, particularly in the middle of the array. The middle of the slice at depth of 1 km has the appropriate resolution, but unreliable results in the boundaries. The horizontal depth slices at 2 and 3 km contain few nodes with appropriate velocity inversion in the core of the array. The first layer has few accepted nodes with appropriate resolution, mostly clustered in the north and north-west of the array. According to Fig. 7, we mask the areas with unreliable resolution in Fig. 6.

4 DISCUSSION

We used local tomography and obtained the 3-D diving *P*-wave velocity structure in the shallow depths of the Dehdasht area (Fig. 4). As depicted by the results, at zero depth, a prominent high-velocity zone is resolved in the inversion, in addition to two low-velocity zones in the middle of the array. The shape of the velocity zones indicates the existence of two synclines in the core of the Dehdasht basin. At zero and 1 km depths, we obtained several clusters with high or low-velocity variations. The 2 and 3 km depth slices show a high-velocity zone in the south of the array and a low-velocity area in the middle. The first layer (height = 1 km) shows a high-velocity zone in the north and west sides of the array and a low-velocity area between them. These velocity variations can be explained by the complex deformation of the Gachsaran formation and the existence of several small anticlines and/or synclines in the area, which are a consequence of the Arabian and Eurasian plate collision that formed the Zagros fold-and-thrust belt.

We compared the tomography results with vertical 2-D seismic reflection profiles provided by NIOC. We selected three lines (8203, 8204 and 8211) that cross the core of the array (see Fig. 6a). All three cross-sections show halokinetic flaps with low-velocity synclines that are surrounded by compressed Gachsaran limestone with high seismic velocity. By plotting the absolute *P*-velocities of the tomography across these profiles (Figs 6b–d), we obtained a very good agreement between the passive seismic tomography results and the active reflection survey.

Our *P*-wave velocity model follows a prominent low-velocity zone throughout all profiles, which is observable down to a depth of 3 km. This low-velocity zone relates to synclines that had also been observed with an active seismic survey from NIOC (Fig. 6). The velocity model in Figs 6(b)–(d) illustrates the existence of two synclines, marked by white and black arrows. The compressed Gachsaran between them has an average velocity of 6 km s^{-1} at a depth of 1 km. Fig. 6(d) shows the penetration of the syncline with an absolute velocity of around 5.8 km s^{-1} in a layer with a velocity of around 6.3 km s^{-1} at a depth of about 2 km. The results of the active field data can show the shape of the west side syncline clearly (white arrow; Fig. 6), while the east side (black arrow) has insufficient resolution. The estimated *P*-velocity explains the shape of both synclines, showing that the east side syncline extends up to a depth of around 3 km with an average velocity of 6.2 km s^{-1} in this depth (Fig. 6c). The location and depth of the estimated velocity anomaly as resolved in this study on the eastern side of the array (black arrow in Fig. 6) is in agreement with the results from a surface wave tomography (Kazemnia *et al.* 2023). The estimated *P*-velocity anomaly on the western side (white arrow in Fig. 6) is only confirmed by the imaged syncline from the NIOC active survey and not the surface wave study.

We observe a lateral smearing in the first layer of the checkerboard test (Fig. S7), which can be explained by the near-vertical direction of the rays and fewer crossings in the near-surface layer. At greater depths, the high frequency of the retrieved body wave, the station spacing, and the geometry of the array limit the depth penetration to around 3–4 km (Fig. S6). The low values of DWS (Figs S6 and 7a–c)

at depths > ∼3 km clearly show poor ray coverage and consequently unreliable results.

By using body waves extracted from the seismic ambient wavefield, we could provide additional details on the shape of the Gachsaran formation in the Dehdasht basin, especially in the middle of the array and depth range of around 0–2 km. However, no additional information about the underlying Asmari formation could be provided. The tomography results of Fig. 4 do not show any velocity increment related to the Asmari formation, indicating that this formation is located deeper. We could clearly reconstruct and pick the *P* wave at a distance of up to around 26.5 km with an appropriate SNR. This is the farthest station distance between available virtual sources and virtual receivers. The quality of the retrieved *P* waves in this study is good enough even at far distances; making the consequence that the applied algorithm has the potential to retrieve the body wave in distances of >26.5 km. However, we have been limited by the size of the array. The longest available ray travelled to a depth of around 3–4 km (Fig. S6), so it could not touch the reservoir limestone. The deeper study of the Dehdasht basin and exploration of the Asmari formation request a bigger array.

5 CONCLUSION

We applied the cross-coherency and polarization approach to continuous seismic ambient noise data to reconstruct the body wave at both near and far distances (∼1.5–26.5 km) in the Dehdasht area. We show that working with a strongly decimated but high-quality data set of around 5 per cent of daily traces is of utmost importance for successful *P*-wave extraction. A careful investigation of these selected traces shows that around 65 per cent of them contain dominant inherent artefacts or later arrivals which complicate the selection of the lower amplitude *P* waves used for tomography.

With the reconstructed diving *P* wave from the seismic ambient wavefield, we imaged the 3-D velocity structure containing the highly attenuating Gachsaran formation. The compatibility of our inversion results with 2-D active seismic profiles demonstrates the application of the interferometry of body wave ambient noise in structural studies. The *P*-velocity outcomes show the existence of two synclines in the Gachsaran formation that have velocity differences of about 0.5 km s^{-1} compared to the compressed Gachsaran areas at equal depths. The tomography results suggest the extension of synclines to a depth of around 3 km.

ACKNOWLEDGMENTS

We are grateful to the National Iranian Oil Company (NIOC) for providing the seismic ambient wavefield data and the supporting information. We thank the editorial board of *Geophysical Journal International*, Prof Gabi Laske, as well as two anonymous reviewers for their comments that helped improve the manuscript. AR conducts this research as part of his PhD at University of Tehran.

DATA AVAILABILITY

The underlying data of this paper cannot be shared publicly due to internal National Iranian Oil Company (NIOC) policies. The data will be shared on reasonable request to the NIOC.

REFERENCE

Abdetedal, M., Shomali, Z. H. & Gheitanchi, M. R. 2015. Ambient noise surface wave tomography of the Makran subduction zone, southeast Iran: implications for crustal and uppermost mantle structures, *Earthq. Sci.,* **28**(4), 235–251.

Barmin, M. P., Ritzwoller, M. H. & Levshin, A. L. 2001. A fast and reliable method for surface wave tomography, *Pure appl. Geophys.,* **158,** 1351–1375.

Bordenave, M. & Hegre, J. 2005. The influence of tectonics on the entrapment of oil in the Dezful Embayment, Zagros Foldbelt, Iran, *J. Petrol. Geol.,* **28**(4), 339–368.

Boué, P., Poli, P., Campillo, M., Pedersen, H., Briand, X. & Roux, P. 2013. Teleseismic correlations of ambient seismic noise for deep global imaging of the Earth, *Geophys. J. Int.,* **194**(2), 844–848.

Dantas, O. A. B., do Nascimento, A. F. & Schimmel, M. 2018. Retrieval of body-wave reflections using ambient noise interferometry using a small-scale experiment, *Pure appl. Geophys.,* **175**(6), 2009–2022.

Draganov, D., Campman, X., Thorbecke, J., Verdel, A. & Wapenaar, K. 2009. Reflection images from ambient seismic noise, *Geophysics,* **74**(5), A63–A67.

Du, Z., Foulger, G. & Mao, W. 2000. Noise reduction for broadband, three-component seismograms using data-adaptive polarization filters, *Geophys. J. Int.,* **141**(3), 820–828.

Eberhart-Phillips, D. 1986. Three-dimensional velocity structure in the northern California Coast Ranges from inversion of local earthquake arrival times, *Bull. seism. Soc. Am.,* **76**(4), 1025–1052.

Eberhart-Phillips, D. 1993. Local earthquake tomography: earthquake source regions, in *Seismic Tomography: Theory and Practice,* ed. Woodhouse, J. H., Blackwell Scientific Publications.

Forghani, F. & Snieder, R. 2010. Underestimation of body waves and feasibility of surface-wave reconstruction by seismic interferometry, *Leading Edge,* **29**(7), 790–794.

Heydarzadeh, K., Hajialibeigi, H. & Gharabeigli, G. 2021. Structural geometry and evolution of the Dehdasht Basin in the Central Zagros fold-and-thrust belt: implications for the timing of oil generation and trap formation, *J. Petrol. Sci. Eng.,* **208**(Part E),.109254.

Heydarzadeh, K., Ruh, J. B., Vergés, J., Hajialibeigi, H. & Gharabeigli, G. 2020. Evolution of a structural basin: numerical modelling applied to the Dehdasht Basin, Central Zagros, Iran, *J. Asian Earth Sci.,* **187,** doi:10.1016/j.jseaes.2019.104088.

Kazemnia, M., Shirzad, T., Shakeri, N., Norouzi, S., Abdollahi, S., Heydarzadeh, K. & Motlagh, S. A. 2023. Shallow crustal model of the DehDasht in Zagros, Iran, using Rayleigh wave tomography, *Phys. Earth planet. Inter.,* **334,**.

Köhler, A., Maupin, V. & Balling, N. 2015. Surface wave tomography across the Sorgenfrei–Tornquist Zone, SW Scandinavia, using ambient noise and earthquake data, *Geophys. J. Int.,* **203**(1), 284–311.

Lashgari, A., Hayhat, M., Vergés, J., Beamud, E., Najafi, M., Khatib, M. & Karimnejad, H. 2020. Age of synorogenic deposits and timing of folding in Dezful embayment, SW Zagros Fold Belt, *Mar. Petrol. Geol.,* **113,** doi:10.1016/j.marpetgeo.2019.104148.

Lehujeur, M., Vergne, J., Schmittbuhl, J., Zigone, D., Le Chenadec, A. & Team, E. 2018. Reservoir imaging using ambient noise correlation from a dense seismic network, *J. geophys. Res.,* **123**(8), 6671–6686.

Liewellyn, P. 1973. Geological compilation map of Deh Dasht (1: 100000), Iranian oil operating Companies, Geological and exploration division.

Macleod, J. & Akbari, Y. 1970. Behbahan geological compilation map 1: 100000, Iran Oil Operating Companies, Tehran.

McMechan, G. A., Clayton, R. W. & Mooney, W. D. 1982. Application of wave field continuation to the inversion of refraction data, *J. geophys. Res.,* **87**(B2), 927–935.

Najafi, M., Vergés, J., Etemad-Saeed, N. & Karimnejad, H. R. 2018, Folding, thrusting and diapirism: competing mechanisms for shaping the structure of the north Dezful Embayment, Zagros, Iran, *Basin Res.,* **30**(6), 1200–1229.

Nakata, N., Boué, P., Brenguier, F., Roux, P., Ferrazzini, V. & Campillo, M. 2016. Body and surface wave reconstruction from seismic noise correlations between arrays at Piton de la Fournaise volcano, *Geophys. Res. Lett.,* **43**(3), 1047–1054.

Nakata, N., Chang, J. P., Lawrence, J. F. & Boué, P. 2015. Body wave extraction and tomography at Long Beach, California, with ambient-noise interferometry, *J. geophys. Res.,* **120**(2), 1159–1173.

Nakata, N. & Nishida, K. 2019, Body wave exploration, in *Seismic Ambient Noise,* pp. 239–266, eds Nakata, N., Gualtieri, L. & Fichtner, A., Cambridge Univ. Press.

Obermann, A., Lupi, M., Mordret, A., Jakobsdóttir, S. S. & Miller, S. A. 2016. 3D-ambient noise Rayleigh wave tomography of Snæfellsjökull volcano, Iceland, *J. Volc. Geotherm. Res.,* **317,** 42–52.

Obermann, A., Molinari, I., Métaxian, J.-P., Grigoli, F., Strauch, W. & Wiemer, S. 2019. Structure of Masaya and Momotombo volcano, Nicaragua, investigated with a temporary seismic network, *J. Volc. Geotherm. Res.,* **379,** 1–11.

Pedersen, H. A. & Colombi, A. 2018. Body waves from a single source area observed in noise correlations at arrival times of reflections from the 410 discontinuity, *Geophys. J. Int.,* **214**(2), 1125–1135.

Planès, T., Obermann, A., Antunes, V. & Lupi, M. 2020. Ambient-noise tomography of the Greater Geneva Basin in a geothermal exploration context, *Geophys. J. Int.,* **220**(1), 370–383.

Poli, P., Campillo, M., Pedersen, H. & Working Group, LAPNET 2012. Body-wave imaging of Earth's mantle discontinuities from ambient seismic noise, *Science,* **338**(6110), 1063–1065.

Retailleau, L., Boué, P., Li, L. & Campillo, M., 2020. Ambient seismic noise imaging of the lowermost mantle beneath the North Atlantic Ocean, *Geophysical Journal International,* **222**(2), 1339–1351.

Riahi, A., Shomali, Z.H., Obermann, A. & Kamayestani, A., 2021. Simultaneous retrieval of body and surface waves in the Dehdasht area, Iran, from the seismic ambient field and the observation of spurious artefacts, *Geophys. J. Int.,* **227**(2), 1193–1203.

Roux, P., Sabra, K. G., Gerstoft, P., Kuperman, W. & Fehler, M. C. 2005. P-waves from cross-correlation of seismic noise, *Geophys. Res. Lett.,* **32**(19),.

Ruigrok, E. 2014. Receiver-pair seismic interferometry applied to body-wave USArray data, *Geophys. J. Int.,* **198**(2), 895–905.

Sabra, K. G., Gerstoft, P., Roux, P., Kuperman, W. & Fehler, M. C., 2005. Surface wave tomography from microseisms in Southern California, *Geophys. Res. Lett.,* **32**(14),.

Salinas, V., Ugalde, A., Kamayestani, A., Jokar, M., Gharibvand, M. M., Villaseñor, A. & Heidari, G. 2019. Designing and testing a network of passive seismic surveying and monitoring in Dehdasht (South Western Iran), *Geophys. Prospect.,* **67**(6), 1652–1663.

Samson, J. & Olson, J. 1981. Data-adaptive polarization filters for multichannel geophysical data, *Geophysics,* **46**(10), 1423–1431.

Shapiro, N. M. & Campillo, M. 2004. Emergence of broadband Rayleigh waves from correlations of the ambient seismic noise, *Geophys. Res. Lett.,* **31**(7), doi:10.1029/2004GL019491.

Shapiro, N. M., Campillo, M., Stehly, L. & Ritzwoller, M. H. 2005. High-resolution surface-wave tomography from ambient seismic noise, *Science,* **307**(5715), 1615–1618.

Shomali, Z. H. & Shirzad, T. 2015. Crustal structure of Damavand volcano, Iran, from ambient noise and earthquake tomography, *J. Seismol.,* **19**(1), 191–200.

Singer, J., Obermann, A., Kissling, E., Fang, H., Hetényi, G. & Grujic, D. 2017. Along-strike variations in the Himalayan orogenic wedge structure in Bhutan from ambient seismic noise tomography, *Geochem. Geophys. Geosyst.,* **18**(4), 1483–1498.

Spica, Z., Perton, M. & Beroza, G. C. 2017. Lateral heterogeneity imaged by small-aperture ScS retrieval from the ambient seismic field, *Geophys. Res. Lett.,* **44**(16), 8276–8284.

Takagi, R., Nakahara, H., Kono, T. & Okada, T. 2014. Separating body and Rayleigh waves with cross terms of the cross-correlation tensor of ambient noise, *J. geophys. Res.,* **119**(3), 2005–2018.

Takagi, R., Nishida, K., Maeda, T. & Obara, K. 2018. Ambient seismic noise wavefield in Japan characterized by polarization analysis of Hi-net records, *Geophys. J. Int.,* **215**(3), 1682–1699.

Thurber, C. 1993. Local earthquake tomography: velocities and Vp/Vs—theory in seismic tomography: theory and practice pp. 563–583 eds Iyer HM, Hirahara K, *Tectonophysics,* **635,** 100–124.

Thurber, C. H. 1983. Earthquake locations and three-dimensional crustal structure in the Coyote Lake area, central California, *J. geophys. Res.,* **88**(B10), 8226–8236.

Thurber, C. & Eberhart-Phillips, D. 1999. Local earthquake tomography with flexible gridding, *Comput. Geosci.,* **25**(7), 809–818.

Toomey, D. & Foulger, G. 1989. Tomographic inversion of local earthquake data from the Hengill-Grensdalur central volcano complex, Iceland, *J. geophys. Res.,* **94**(B12), 17 497–17 510.

Zhang, J. & Gerstoft, P. 2014. Local-scale cross-correlation of seismic noise from the Calico fault experiment, *Earthq. Sci.,* **27**(3), 311–318.

SUPPORTING INFORMATION

Supplementary data are available at *GJI* online.

Please note: Oxford University Press is not responsible for the content or functionality of any supporting materials supplied by the authors. Any queries (other than missing material) should be directed to the corresponding author for the paper.